# Low-resistance contact in MoSe<sub>2</sub>-based solid-state thermionic devices

Md Golam Rosul<sup>1</sup>, Xiaoming Wang<sup>2,3</sup>, Keivan Esfarjani<sup>4,5,6</sup>, Mona Zebarjadi<sup>1,5,\*</sup>

<sup>1</sup>Department of Electrical and Computer Engineering, University of Virginia, Charlottesville, VA 22904, United States

<sup>2</sup>Department of Physics and Astronomy, University of Toledo, Toledo, OH 43606, USA

<sup>3</sup>Wright Center for Photovoltaic Innovation and Commercialization, University of Toledo, Toledo, OH 43606, USA.

<sup>4</sup>Department of Mechanical and Aerospace Engineering, University of Virginia, Charlottesville, VA 22904, United States

<sup>5</sup>Department of Materials Science and Engineering, University of Virginia, Charlottesville, VA 22904, United States

<sup>6</sup>Department of Physics, University of Virginia, Charlottesville, VA 22904, United States \*Corresponding author: <u>mz6g@virginia.edu</u>

#### **Abstract:**

Solid-state thermionic structures made out of layered van der Waals heterostructures have shown promising thermal to electrical energy conversion efficiencies theoretically. In this work, we further study these structures using first-principles calculations combined with Green's function method. By calculating the electron-phonon relaxation length, we confirm ballistic transport in these structures. We study the effect of the number of layers, the energy barrier, and the asymmetry of the contacts on the performance of MoSe<sub>2</sub> based thermionic converters. We show that the key to high-performance thermionic diodes is to make a low-energy barrier, low-resistance metallic contacts and we identify copper as the optimum metallic contact to MoSe<sub>2</sub> based devices.

We further show that, unlike the vacuum-based thermionic diodes, asymmetry does not result in improved performance within the linearized transport theory.

#### I. Introduction

The advent of low-power portable and wearable electronics signifies the need for mesoscale power generators and coolers [1–5]. Mechanical generators cannot be miniaturized to such scales and hence currently we rely on batteries to power portable electronics. Thermionic power generators and coolers can be built with nanoscale thickness and provide a solid-state solution for energy scavenging and integrated cooling.

A thermionic converter essentially is a heat engine that converts thermal energy directly to electricity using electrons as the working fluid. Similar to most other heat engines, thermionic devices can operate either as power generators or coolers. There are two main types of thermionic converters: vacuum state thermionic (VSTI) converters and solid-state thermionic (SSTI) converters [1,2,6–8]. In the power generation mode, heat is used to increase the energy of electrons in the cathode. The hot electrons with energies higher than the energy barrier can pass above the barrier with a Richardson flux. These electrons are then collected by a colder anode. A part of the thermal energy is thus converted directly to electricity and the rest is rejected as heat to the cold side. The energy barrier in the case of VSTI is the cathode work function, which is on the order of a few electron volts

in typical metals. Therefore, vacuum thermionic power generators can only operate at very high temperatures. Also, the need for a vacuum in a VSTI restricts direct access to the electrodes. To overcome these difficulties, Shakouri and Bowers [1] proposed a single-layer solid-state thermionic in 1997 diodes in which the vacuum is replaced by a semiconducting material. In this structure, the semiconductor layer is the energy barrier that an electron experiences. In the following year, Mahan proposed the idea of using multi-layer barriers in which each layer maintains a small temperature difference [2,7]. Electrons in a solid-state thermionic device can face an effective energy barrier height on the order of meV as the energy barrier is the difference between the electron affinity of the semiconductor and the work function of the metal. This is compared to a few eVs barrier heights in a vacuum thermionic device. Hence, SSTICs can operate at much lower temperatures compared to VSTICs. Our previous theoretical work focusing on the mathematical optimization of solid-state thermionic devices concluded that for optimum performance the optimum barrier height should be on the order of a few K<sub>B</sub>T [9].

The transport inside the semiconducting layer of an SSTIC has to be ballistic to avoid electron-phonon thermalization. To maintain ballistic transport in a solid-state thermionic device, the semiconducting layer thickness should be lower than the electron mean free path. At the same time, a minimum barrier thickness is needed to suppress the tunneling of electrons in the device. If electrons of energy lower than the

semiconductor barrier height tunnel through, they carry less energy if their energy is above the Fermi level, and will carry negative heat (a rare event) if their energy is below the Fermi level. This leads to a lower Seebeck as our previous and present studies have shown. Hence, SSTICs are considered nanoscale devices appropriate for integrated circuits [6,10,11]. At such small scales, the main challenge of SSTICs, is their thermal leakage [12]. To maintain a noticeable temperature difference at such a small length scale, the thermal conductance of an SSTIC needs to be very small. Our recent work has shown that the thermal conductance of a solid-state thermionic device should be smaller than 0.1 MWm<sup>-2</sup>K<sup>-1</sup> to obtain reasonable efficiencies [9]. To our best knowledge, within ordered and nonporous systems, this very small thermal conductance is only possible in the van der Waals heterostructures [13,14] due to their weak van der Waals interactions compared to covalent bonding [15]. In one work, our group showed that five layers of black phosphorene sandwiched between gold and graphene has a thermal conductance value of 4-6 MWm<sup>-2</sup>K<sup>-1</sup> [16]. In another work our group theoretically calculated a thermal conductance value of 16 MWm-2K-1 for Sc-WSe2-MoSe2-WSe2-Sc structure [17]. Other weakly bonded structures also demonstrated extremely low thermal conductance values. It was shown that interfacial thermal conductance between seven layers of MoS2 and crystalline silicon (c-Si) is smaller than 1MWm<sup>-2</sup>K<sup>-1</sup>. [18] In another work, it was experimentally shown that 5-10 MWm<sup>-2</sup>K<sup>-1</sup> thermal conductance can be obtained in the van der Waals structure [19]. A theoretical work based on molecular dynamic simulation obtained a slightly higher thermal conductance value of 17 MWm-<sup>2</sup>K<sup>-1</sup> for both graphene-WSe<sub>2</sub>-graphene and graphene-MoSe<sub>2</sub>-graphene structures. In another experimental work, a very low thermal conductance value of 0.5 MWm<sup>-2</sup>K<sup>-1</sup> was estimated for a graphene-WSe<sub>2</sub>-graphene structure [20]. In addition, in a van der Waals heterostructure, the barrier height, which plays a significant role in improving the device performance can be tuned by changing the number of layers in the heterostructure from 0 in the tunneling regime (one layer) to the bulk bandgap value for a large enough number of layers (typically 10 layers) [16]. In recent years, these two important features of van der Waals heterostructure have renewed interest in solid-state thermionic devices [5,16,21–24].

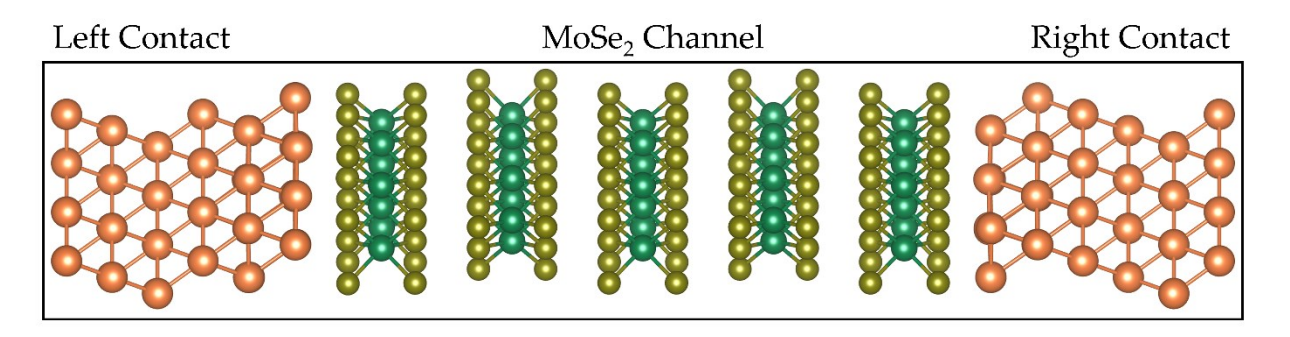


Figure 1. Ball stick model of a metal-MoSe2-metal device configuration.

In this work, we study thermionic transport properties of metal-MoSe<sub>2</sub>-metal structure as shown in Fig. 1 by using density functional theory (DFT)-based first-principles calculations combined with real-space Green's function (GF) transport formalism. MoSe<sub>2</sub>,

a layered two-dimensional (2D) transition metal dichalcogenides (TMDs) used as the semiconducting material in these calculations. An advantage of layered TMD materials such as MoSe<sub>2</sub> is that the saturated covalent bonds within one layer and noncovalent binding between the layers allow for atomically sharp and stress-free interfaces between similar or dissimilar materials [25]. Another important feature of MoSe<sub>2</sub> is that the electronic properties depend on the number of layers. For example, bulk MoSe<sub>2</sub> has an indirect bandgap of 0.85 eV while monolayer MoSe<sub>2</sub> has a direct bandgap of 1.55 eV [26,27]. Moreover, the thermal transport in MoSe<sub>2</sub> in the cross-plane direction is greatly reduced due to the lack of covalent bonding between layers. These electrical and thermal properties make MoSe<sub>2</sub> a suitable material for designing efficient solid-state thermionic devices.

In nanoscale electronics contacts often play a more important role than the semiconducting material itself [28,29]. While contact in Si-based devices is no longer challenging after many years of engineering optimization, contact to nanoscale electronic devices based on 2D TMD materials has become a major challenge [30–33]. A strong interface bonding creating interface states that pin the Fermi level [34] or a weak bonding creating a potential step due to Pauli repulsion [35,36] at the interface can cause high barrier height between the metal contact and the 2D TMDs. Therefore, for the applicability of novel 2D TMDs such as MoSe<sub>2</sub> as nanoscale devices, a comprehensive study of metal contacts to the 2D TMDs is very important. There are several ways to

extract the metal-2D TMD barrier height [37]. In this work, we extract the barrier height between metal-MoSe<sub>2</sub> from the electronic transmission function. We first systematically study the contact between MoSe<sub>2</sub> and various metals (Au, Pt, Ni, Cu). We then study thickness dependence of the contact and identify Ohmic contacts. We also study the thermionic performance of these structures.

Next, we investigate the effect of asymmetric metallic contact on the performance of SSTI devices. In a VSTI device, the output power is proportional to the work function difference between the cathode and the anode. Hence, it is desired to have asymmetric electrodes wherein the cathode has a larger work function compared to the anode [38–40]. The solid-state thermionic devices designed so far have similar metallic contact as cathode and anode [5,16,21]. Therefore, the effect of asymmetric metallic contact with different work functions on the device performance is unknown. In our work, we evaluate the performance of two sets of asymmetric structures (Au-MoSe<sub>2</sub>-Pt and Cu-MoSe<sub>2</sub>-Au) and compare their performance with their symmetric counterparts (Au-MoSe<sub>2</sub>-Au, Pt-MoSe<sub>2</sub>-Pt, and Cu-MoSe<sub>2</sub>-Cu).

## II. Computational Method

#### **DFT** calculation details

To model the proposed device, we use open boundary conditions along the z-axis, while periodicity is imposed in the xy plane. To study the structural and electronic properties of the metal<sub>1</sub>-MoSe<sub>2</sub>-metal<sub>2</sub> van der Waals heterostructure, we used the state-of-the-art

density functional theory (DFT) based first-principles calculations combined with real-space Green's function (GF) transport formalism, as implemented in the SIESTA package [41]. We used the exchange-correlation functional of Perdew-Burke-Ernzerhof [42] revised for solids [43] and standard basis set, namely, double zeta plus polarization (DZP). Real-space mesh cutoff energy was set to 300 Ry. A single k point in the cross-plane direction whereas a 5×5 k mesh in the basal plane was used for the Brillouin zone sampling.

## Making and optimization of the SSTI structures

We first optimized the lattice parameters of Au, Pt, Cu, Ni, and MoSe<sub>2</sub> separately for the purpose of obtaining the optimized in-plane lattice parameters of the structures. The optimized in-plane lattice constants are 4.08 Å, 3.93 Å, 3.61 Å, 3.52 Å, 3.31 Å respectively. Our calculated in-plane lattice parameter of MoSe<sub>2</sub> matches the reported value in the literature [21,44–46]. Therefore, the in-plane lattice parameters of the relaxed <111> plane of the metallic contacts (Au, Pt, Cu, Ni) are 2.885 Å, 2.779 Å, 2.553 Å, and 2.489 Å respectively. In the structures, 3-6 layers of MoSe<sub>2</sub> are sandwiched between 6 layers of <111> plane of the metallic contacts. In the DFT-GF method, the electrodes are assumed to be semi-infinite, and using 6 layers we achieved convergence in the results. The transport properties will not change when the number of layers of the metallic contact increased beyond 6. The in-plane lattice parameters of the structures are fixed to the optimized metal <111> plane for the symmetric structures while the average of relaxed

metal<sub>1</sub> <111> plane and relaxed metal<sub>2</sub> <111> plane for asymmetric structures and in-plane MoSe<sub>2</sub> lattice parameters were adapted accordingly  $(2\sqrt{3}a_{Au/Pt<111>} = 4a_{Cu/Ni<111>} =$  $3a_{MoSe_2}$ , a is the lattice constant) to minimize the strain. Thus, the MoSe<sub>2</sub> in the Au-MoSe<sub>2</sub>-Au, Pt-MoSe<sub>2</sub>-Pt, Cu-MoSe<sub>2</sub>-Cu, Ni-MoSe<sub>2</sub>-Ni, Au-MoSe<sub>2</sub>-Pt, and Au-MoSe<sub>2</sub>-Cu structures experience 0.65% tensile, 3% compressive, 2.8% tensile, 0.26% tensile, 1.24% compressive and 1.73% tensile strain respectively. It is known that the tensile strain increases the bandgap while the compressive strain decreases the bandgap [47,48]. After forming the devices, all the structures are optimized again. In the optimization process, the atomic positions of two inner layers of metal from each side along with all the MoSe<sub>2</sub> layers, called the channel region, are allowed to relax without any constraints along the cross-plane direction until the forces on all atoms are less than 0.01 eV/Å while the atomic positions of the outer four metallic layers from each side, considered as left and right contacts, are kept fixed. We use the non-local van der Waals DFT functional (vdW-DFoptb86) [49,50] to correctly take the van der Waals interaction into account during the structure optimization.

## **Electron transport calculations**

The electronic transport properties of the SSTI devices are studied by using density functional theory (DFT)-based first-principles calculations combined with real-space Green's function (GF) transport formalism. The transport properties calculations of the optimized structures are performed using PBE functionals. Although the GGA functional

such as PBE used in this work underestimate the bandgaps, due to the presence of two metallic electrodes which strongly screen the Coulomb interaction, the bandgap becomes small so that we have a cancellation of this underestimation error. This was confirmed in our previous work by comparing with the GW calculations on the same structure [21]. The electron transmission functions are calculated using real-space Green's function method as in the TranSIESTA implementation [51]. TranSIESTA deals fully with the atomistic structure of the whole system, treating both the contact and the electrodes on the same footing. After calculating the electron transmission function using TranSIESTA, the transport coefficients are obtained using the linear response approximation [52]:

Conductance, 
$$G = q^2 L_0$$

Seebeck coefficient, 
$$S = L_1/qTL_0$$

Electronic thermal conductance,  $\kappa_{el} = (L_2 - L_1^2/L_0)/T$ 

where, 
$$L_n = 2/h \int dE T(E) (E - \mu)^n (-\frac{\delta f}{\delta E})$$

where q is the electron charge, and f is the Fermi-Dirac distribution function.

# Electron-phonon scattering rate and mean free path (MFP) calculation

We compute the electron-phonon scattering rate and the MFPs in bulk MoSe<sub>2</sub> using the first principles. The equilibrium properties of electrons and phonons are calculated using

the density functional theory (DFT) and density functional perturbation theory (DFPT)

as implemented in the QUANTUM ESPRESSO package [53]. The norm-conserving

pseudopotentials [54] with the Perdew-Burke-Ernzerhof (PBE) [55] functional for the

exchange-correlation is used. A 6×6×2 and a 12×12×4 Monkhorst-Pack k-point mesh are

used for the self-consistent and non-self-consistent field calculations, respectively and the

cutoff energy of the plane wave is chosen as 60 Ry. The convergence threshold of energy

is set to be 10<sup>-12</sup> Ry. Lattice was relaxed with the force convergence threshold of 10<sup>-4</sup>

Ry/Bohr. The obtained relaxed lattice constant of bulk MoSe2 in the hexagonal structure

are a=b=3.31 Å and c=12.89 Å. The dynamical matrices and phonon perturbations are

computed on a 6×6×2 q point mesh in the phonon calculations. To obtain the electron-

phonon scattering rates, the EPW package [56] is employed to interpolate the electron-

phonon coupling matrices as well as electron and phonon eigenvalues obtained by DFT

and DFPT calculations from coarse to fine k and q point meshes (30×30×30) using the

Wannier interpolation scheme [57]. The electron group velocities are obtained from the

BoltzTrap package [58]. Finally, the MFP is obtained by multiplying the electron-phonon

scattering rates with the group velocities.

III. Results and Discussion

Metallic contact for MoSe<sub>2</sub> based electronics

11

Today, a large number of 2D layered materials are identified. Monolayers can be peeled off and stacked on top of each other to form a variety of desired thermal, optical, electronic properties, opening the possibility of nanoscale electronic devices for a variety of medical, environmental, security, and sensing applications. A challenge to make the desired planar electronics out of these lego-type stacked layers is the formation of lowresistance metallic contacts. The contact resistance and in particular the potential barrier height are important parameters for thermionic transport as well as making metallic contact in a 2D planar device consisting of TMD materials. To form low-resistance contact between the metal and the 2D TMD materials, the potential barrier height needs to be very low (on the order of k<sub>B</sub>T). We calculate the potential barrier height of metal-MoSe<sub>2</sub>metal SSTI structure consisting of 5 layers of MoSe<sub>2</sub> for different metals (Au, Pt, Cu, Ni) as well as Au-MoSe<sub>2</sub>-Au structure for 3-6 layers of MoSe<sub>2</sub>. A simple way to estimate the potential barrier height is the Schottky-Mott (SM) rule,  $E_b = I-W$  (for holes) or  $E_b = W-\chi$ (for electrons), where E<sub>b</sub> is the potential barrier height, W is the metal's work function, I is the ionization potential of the semiconductor, and  $\chi$  is the electron affinity of the semiconductor. However, this simple and approximate method does not always predict the correct potential barrier height [16] and certainly does not work well for our studied structures. Here, we use a more accurate first-principles-based method to extract the potential barrier height. First, we use first-principles calculations to relax the metal-MoSe<sub>2</sub>-metal structure. Next, we calculate the transmission function of the structure using Green's function method (see Fig. S1 from Supplementary Information). We then calculate the  $E_b$  for electrons by measuring the  $E_c$ - $E_F$  for electrons and  $E_F$ - $E_v$  for holes from the transmission function, where  $E_F$  is the Fermi energy,  $E_c$  ( $E_v$ ) refers to the corresponding energy levels at the start of non-zero transmission above (below) the Fermi level. As an example, the work function of gold (111) is 5.1 eV and the ionization potential

Table I. Calculated bandgap & barrier height of metal-5 MoSe<sub>2</sub>-metal SSTI structure

Metal contact	Au	Pt	Cu	Ni
5L MoSe <sub>2</sub>	0.89	0.89	0.87	0.80
Transmission gap (eV)				
Barrier Height (eV)	0.26	0.42	0.10	0.30
(Calculated)	(n type)	(p type)	(n type)	(n type)
Barrier Height (eV)	0-0.14	0-0.12	0.62 (n-type)	0-0.20
(SM rule)	(p-type)	(p-type)	0.14(p-type)	(p-type)

of a single layer of MoSe<sub>2</sub> is 5.22 eV [59]. Therefore, the SM rule predicts a barrier height of 0.12 eV and a p-type transport, whereas our first-principles calculation indicates a barrier height of 0.26 eV and an n-type transport. Similarly, the calculated barrier height is n-type for Cu, while the SM rule predicts p-type barrier height. Table I summarizes the calculated potential barrier height of metal-5 MoSe<sub>2</sub>-metal structure, and a range of barrier height predicted by the SM rule for Au, Pt, Cu, Ni. The table also shows the

transmission gap  $E_g$  for MoSe<sub>2</sub> in each structure, where  $Eg = E_c - E_v$ . We note that it is more difficult to extract this information from the local density of states as the screening effect of the metal on its adjacent layer results in a tail in the density of states, hence we define the transmission gap instead of bandgap. From the calculated potential barrier heights listed in the table, we see that Cu makes low energy contact for MoSe<sub>2</sub>, which becomes n-type, with a barrier height of 0.10 eV. Therefore, it is expected that the Cu-MoSe<sub>2</sub> based SSTI device to have the highest electrical conductance among the studied metals.

Table II. Variation of barrier height with the numbers of MoSe<sub>2</sub> layers

Number of layers	3 layers	4 layers	5 layers	6 layers
Barrier Height (eV)	0.20	0.30	0.33	0.40

Next, we study the effect of the number of MoSe<sub>2</sub> layers on metal-MoSe<sub>2</sub> contact resistance. The energy states of the metal significantly affect the energy states of the adjacent layers. This screening effect damps with distance and hence it is expected that the barrier height to be dependent on the number of layers. Here, we calculate the potential barrier height for Au-MoSe<sub>2</sub>-Au SSTI structure where the number of layers of MoSe<sub>2</sub> varied from 3 to 6 layers in the heterostructure. Table II shows the potential barrier height for the Au-3-6 MoSe<sub>2</sub>-Au SSTI structure. We see that the SSTI structure with 3 layers of MoSe<sub>2</sub> shows the lowest barrier height of 0.2 eV, therefore, expected to show the highest electrical conductance as more electrons will overcome the energy barrier. We

note that the transmission gap closes for 1 and 2 layers and transport is dominantly through tunneling.

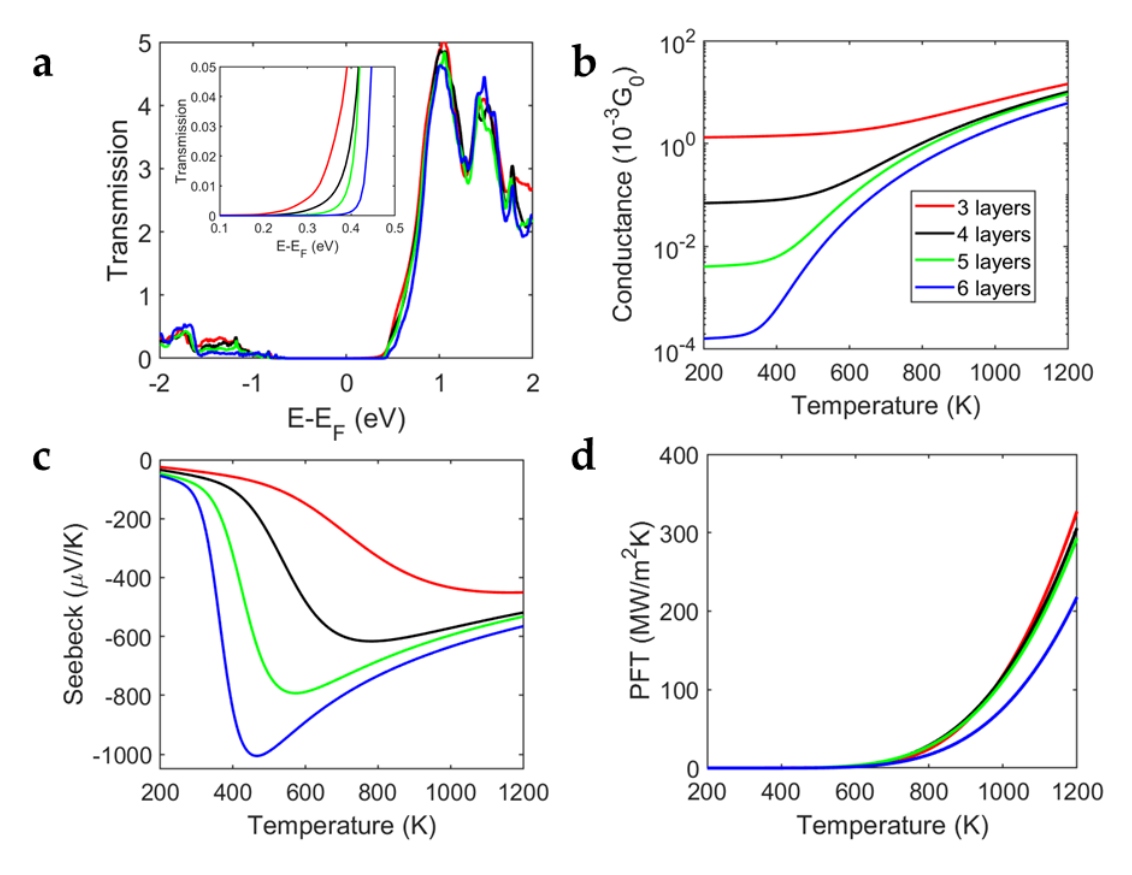


Figure 2. (a) Transmission function (b) electrical conductance (c) Seebeck coefficient and (d) power factor times temperature of heterostructure containing 3-6 layers of MoSe<sub>2</sub>. The inset of figure (a) shows a closeup of the transmission functions.

Next, we evaluate the performance of the Au-3-6 MoSe<sub>2</sub>-Au SSTI structure. Fig. 2(a) shows the transmission function of the structure containing 3-6 layers of MoSe<sub>2</sub>. Fig. 2(b) and Fig. 2(c) show the electrical conductance ( $\sigma$ ) and Seebeck coefficient (S) of all the structures. The electrical conductance of the structure with 3 layers of MoSe<sub>2</sub> is maximum and electrical conductance decreases as the number of MoSe<sub>2</sub> layers in the structure increases. This is consistent with the barrier height of the structures as shown in table 2.

Also due to the increase in the number of thermally excited electrons, the electrical conductance increases as the temperature increases as shown in Fig. 2(b). The Seebeck coefficient increases with the number of MoSe<sub>2</sub> layers in the heterostructure because the transmission gap increases with the number of layers. The power factor times temperature (PFT= $\sigma S^2 T$ ) is a parameter that is used to characterize the power generated by the SSTI device is shown in Fig. 2(d) for all the structures. The PFT is optimum for the structure with 3 layers of MoSe<sub>2</sub> at the temperature range of 200-500K and 970-1200K while structures with 4 and 5 layers of MoSe<sub>2</sub> show optimum PFT at the temperature range of 500-750K and 750-970K respectively. A breakdown of the PFT for each of these temperature ranges is shown in supplementary materials figure S2. The maximum power factor for the structure with 3 layers of MoSe<sub>2</sub> is 327 MWm<sup>-2</sup>K<sup>-1</sup> at 1200K. For comparison, our previously calculated structure Au-Gr-3 WSe<sub>2</sub>-Gr-Au, Pt-Gr-3 WSe<sub>2</sub>-Gr-Pt showed a PFT of 0.83 MWm<sup>-2</sup>K<sup>-1</sup> and 60 MWm<sup>-2</sup>K<sup>-1</sup> respectively at 800K [5] and Sc-WSe<sub>2</sub>-3 MoSe<sub>2</sub>-WSe<sub>2</sub>-Sc showed a PFT of 427 MWm<sup>-2</sup>K<sup>-1</sup> at 1200K [21]. Note that the unit used here is for 2D structures and is different to those used for bulk thermoelectric power factor.

## Asymmetric MoSe<sub>2</sub> based SSTI

In VSTI, two dissimilar metals with work function differences larger than 1 eV are used as cathode and anode and the output power is proportional to the work function difference between the metals. The solid-state thermionic devices designed so far have

similar metallic contact as cathode and anode [5,16,21]. Therefore, the effect of asymmetric metallic contact with different work functions on the device performance is not understood. In this section, we evaluate and compare the performance of two sets of symmetric and asymmetric SSTI devices. In the first set of calculations, we evaluate the performance of symmetric Au-5 MoSe<sub>2</sub>-Au, symmetric Pt-5 MoSe<sub>2</sub>-Pt, and asymmetric Au-5 MoSe<sub>2</sub>-Pt structures and in the second set of calculations, we evaluate the performance of symmetric Au-3 MoSe<sub>2</sub>-Au, symmetric Cu-3 MoSe<sub>2</sub>-Cu, and asymmetric Au-3 MoSe<sub>2</sub>-Cu structures. Since in the previous part we identified 3-5 layers as optimally performed devices, for all calculations in this section, 3 or 5 layers of MoSe<sub>2</sub> are used.

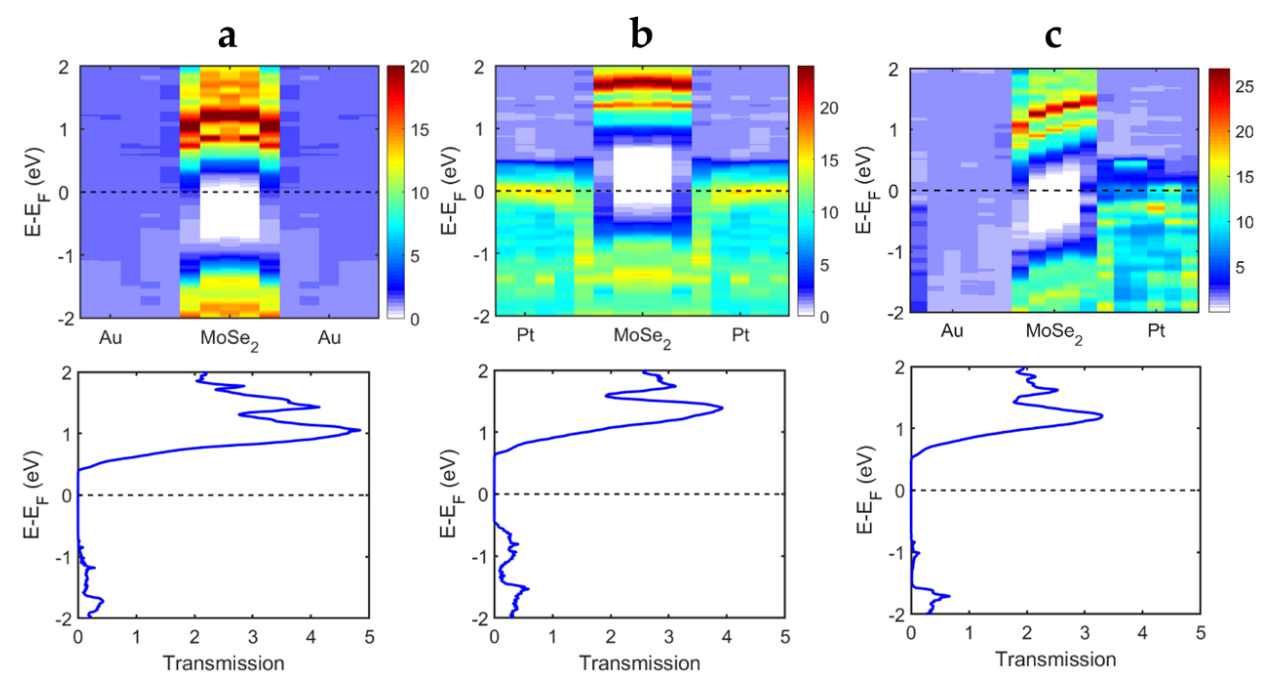


Figure 3. Local density of states of (a) Au-5 MoSe<sub>2</sub>-Au (b) Pt-5 MoSe<sub>2</sub>-Pt (c) Au-5 MoSe<sub>2</sub>-Pt and their corresponding transmission functions.

Fig. 3 shows the local density of states (LDOS) of symmetric gold, symmetric platinum, and the asymmetric structure with one side gold and another side platinum and their corresponding transmission functions. Gold and platinum are chosen since they have similar work functions. From the LDOS we see that the Fermi level E<sub>F</sub> is located near the

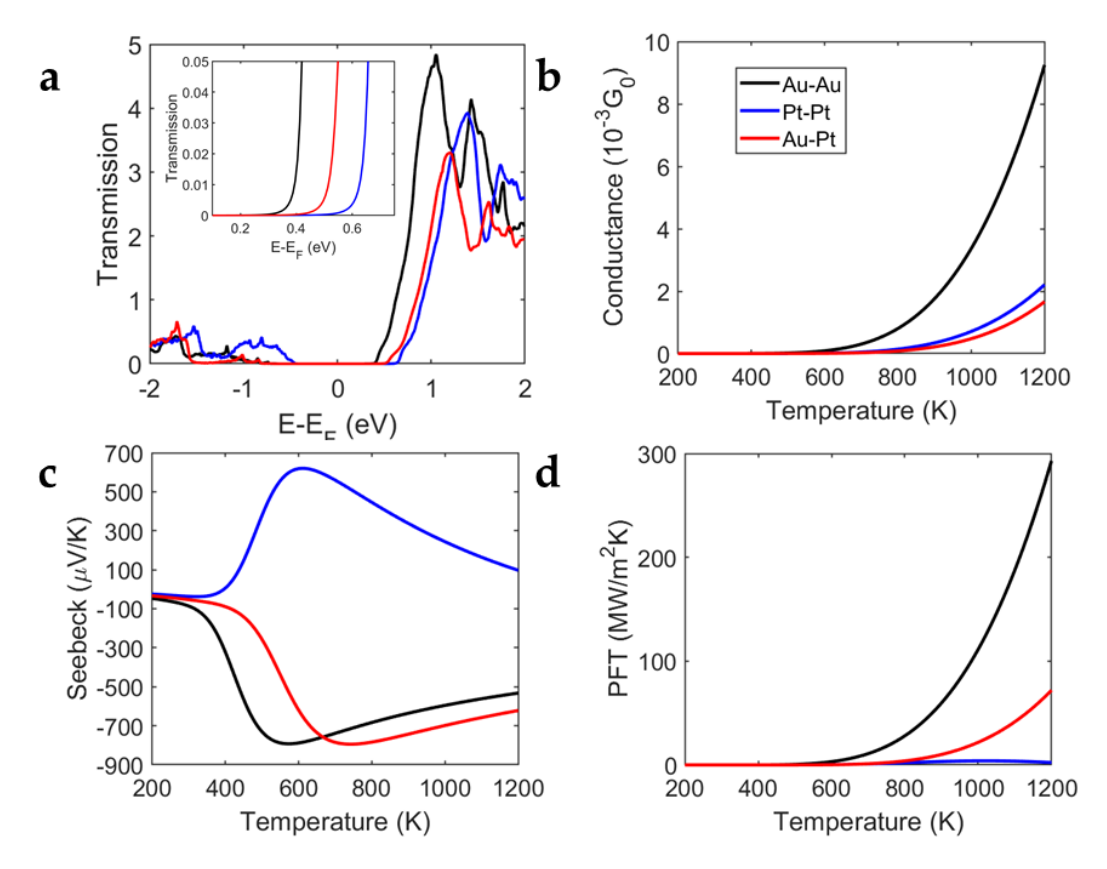


Figure 4. Transmission function (b) Seebeck coefficient (c) electrical conductance and (d) power factor times temperature of the gold, platinum, and gold-platinum asymmetric structure containing 5 layers of MoSe<sub>2</sub>. The black line represents the gold structure, the blue line represents the platinum structure, and the red line represents the gold-platinum asymmetric structure. The inset of figure (a) shows a closeup of the transmission functions.

conduction band of the gold and gold-platinum asymmetric structure which means these structures are n-type while the Fermi level of the platinum structure is located near the valence band making it p-type. The transmission function, Seebeck coefficient, electrical conductance, and the power factor times temperature for all three structures are shown

in Fig. 4. As can be seen from the LDOS and the transmission function, the gold structure has a lower barrier height compared to the other two structures. Therefore, the gold structure shows higher electrical conductance values as shown in Fig. 4(b). The platinum structure shows a positive Seebeck coefficient while the gold and the gold-platinum asymmetric structure show a negative Seebeck coefficient (Fig. 4(c)) which is consistent with the p-type and n-type barrier height of the respective structures. The platinum structure shows a maximum Seebeck coefficient of 620 µV/K at 620K while the maximum Seebeck coefficient of the gold and gold-platinum asymmetric structure is -792 µV/K and -795 μV/K at 572K and 740K respectively. The presence of the bandgap in these structures contributes to the large Seebeck coefficients. The PFT of all three structures is shown in Fig. 4(d). The high electrical conductance due to low barrier height and the high Seebeck coefficient of the gold structure results in the highest PFT at high temperatures. The low electrical conductance combined with the low Seebeck coefficient makes the platinum structure worst performing among the three structures while the PFT of the platinumgold asymmetric structure is in between the PFT of the gold and platinum structure.

In the previous set of calculations, we see that while the gold and gold-platinum asymmetric structure is n-type, the platinum structure is p-type. For the next set of calculations, we find another metal contact that has a very close work function to gold and creates a structure that is n-type doped. We choose copper for this calculation which

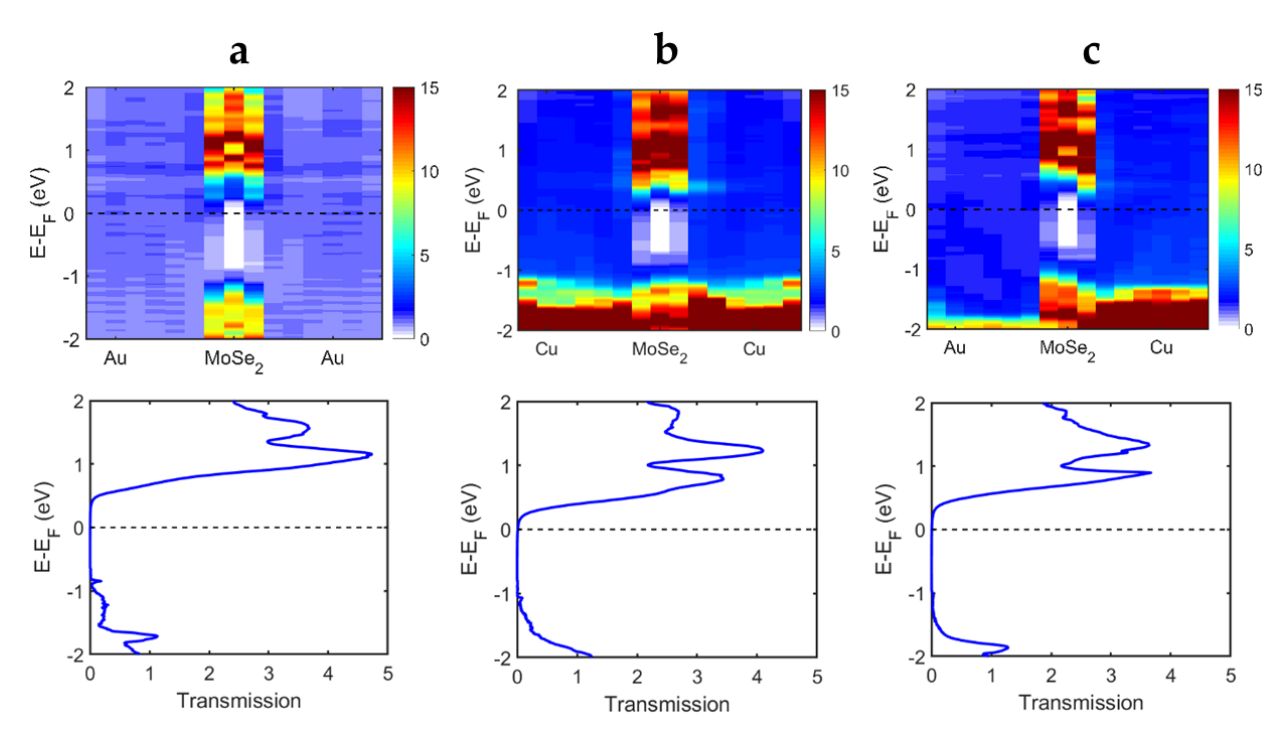


Figure 5. Local density of states of (a) Au-3 MoSe<sub>2</sub>-Au (b) Cu-3 MoSe<sub>2</sub>-Cu (c) Au-3 MoSe<sub>2</sub>-Cu and their corresponding transmission functions.

has a work function value of 4.53-5.10 eV. Therefore, Au-3 MoSe<sub>2</sub>-Au, Cu-3 MoSe<sub>2</sub>-Cu are the symmetric structures and Au-3 MoSe<sub>2</sub>-Cu is the asymmetric structure for these calculations. The local density of states and the corresponding transmission function of symmetric gold, symmetric copper, and a gold-copper asymmetric structure are shown in Fig. 5. The Fermi level E<sub>F</sub> for all these structures is close to the conduction band which means all the structures are n-type doped. The energy barrier height of the copper structure is significantly lower than the other two structures. The electrical conductance of all the structures is shown in Fig. 6(b). The electrical conductance of the copper structure is very high compared to the other two structures due to the significantly lower barrier height. The n-type doping of all the structures can be further verified by the

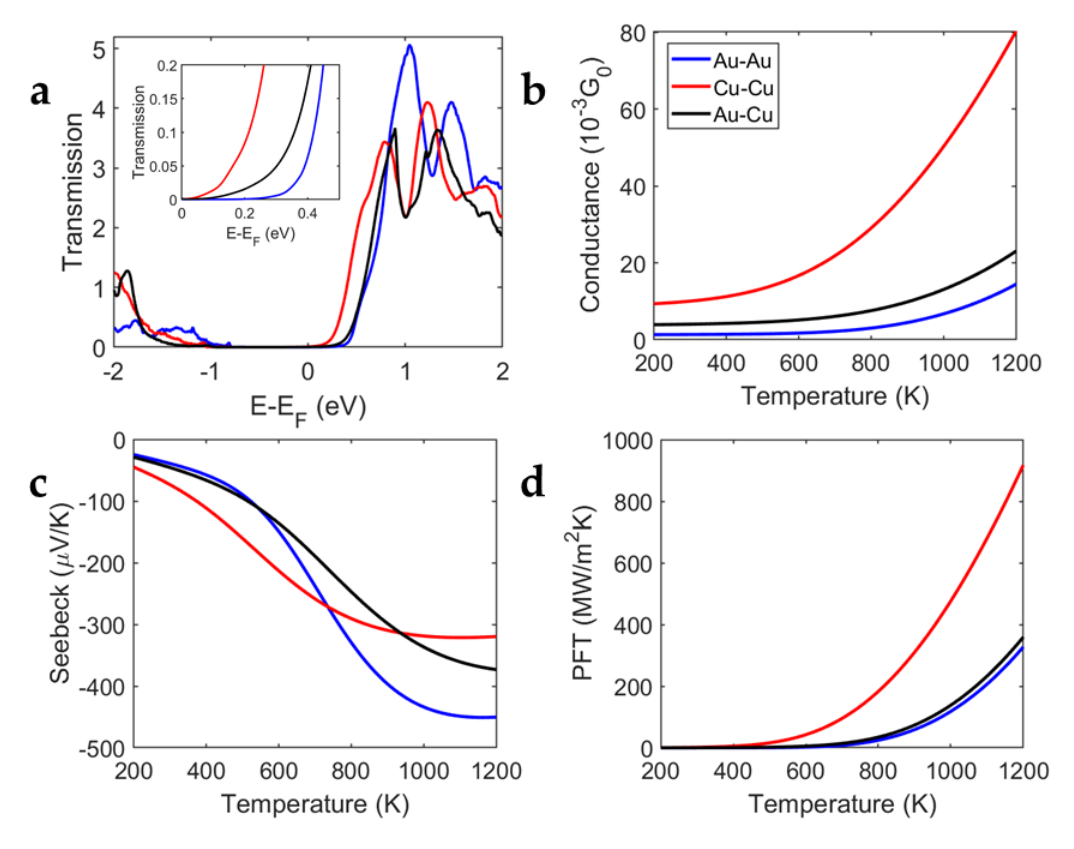


Figure 6. (a) Transmission function (b) electrical conductance (c) Seebeck coefficient and (d) power factor times temperature of the gold, copper, and gold-copper asymmetric structure containing 3 layers of MoSe<sub>2</sub>. The blue line represents the gold structure, the red line represents the copper structure, and the black line represents the gold-copper asymmetric structures. The inset of figure (a) shows a closeup of the transmission functions.

negative Seebeck coefficient as shown in Fig. 6(c). The maximum Seebeck coefficient of the gold, copper, and gold-copper asymmetric structures are -451  $\mu$ V/K, -321  $\mu$ V/K, and -373  $\mu$ V/K respectively at 1200 K. The PFT of the gold, copper, and gold-copper asymmetric structures are 327 MWm<sup>-2</sup>K<sup>-1</sup>, 917 MWm<sup>-2</sup>K<sup>-1</sup>, and 373 MWm<sup>-2</sup>K<sup>-1</sup> respectively

at 1200 K (Fig. 6(d)). The PFT of the copper structure is the highest among all the SSTI structures have been calculated so far [5,21,60].

We note that the transport properties of the asymmetric structure are always in between the two symmetric ones. The only exception is the Seebeck coefficient in the range of 600K to about 1000K wherein the asymmetric structure shows a Seebeck coefficient smaller than both symmetric counterparts.

From these two sets of calculations, we see that the PFT of the asymmetric structure is in between the PFT of their symmetric counterpart. Although the asymmetry of the metallic contact improves the performance of VSTI devices, the asymmetry of metallic contact does not affect the performance of SSTI devices. This is possibly due to the difference in the operating temperature and barrier height between the two types. One has to keep in mind that given the nanoscale thickness of these devices only a very small temperature difference can be maintained between the electrodes. Since the optimal operating temperatures of symmetric structures are very different, the performance of the asymmetric structure can never be superior to the symmetric ones unless their barrier height is the same. Whereas the VSTI barrier height is few eVs, the ideal barrier height of SSTIs is only on the order of meV. Given the small temperature difference which can be maintained in these structures, we can linearize the theory of thermionic transport, define

equivalent Seebeck coefficient and power factor. Upon doing so, the asymmetric structure shows average properties, in between the two symmetric counterparts similar

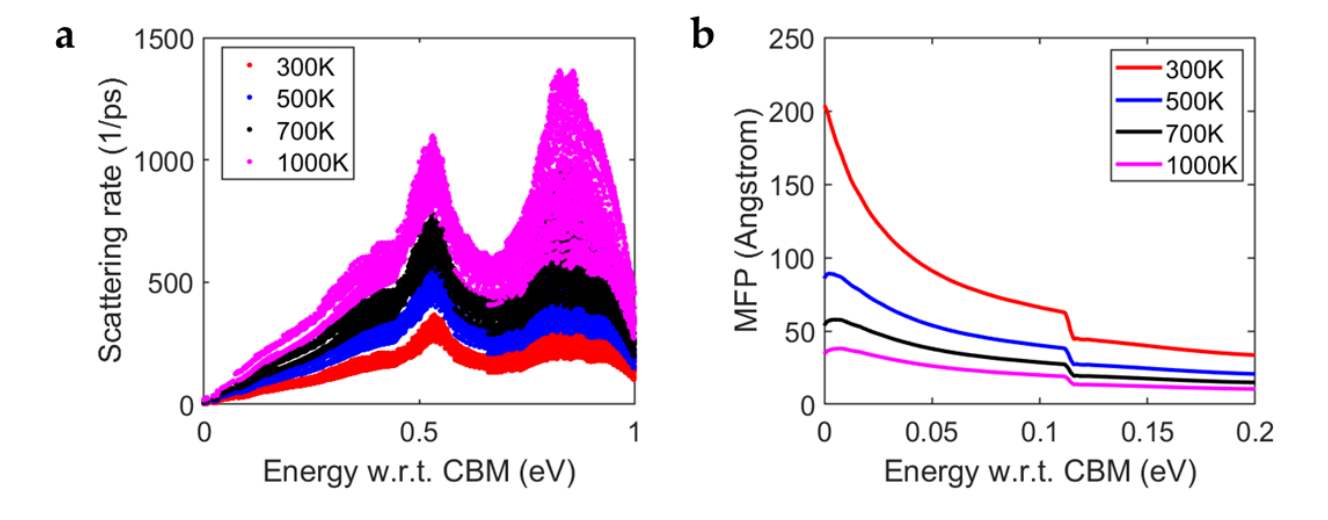


Figure 7. (a) Electron-phonon scattering rate for bulk MoSe2. (b) Electron mean free path calculated along the z-axis.

to how averaging is done in thermoelectric structures. The most important parameter in these structures seems to be the barrier height itself. The lower the barrier height, the higher the power factor. We know the optimum barrier height is about  $2K_bT$  which corresponds to 50 meV at room temperature and 100 meV at 600K. The latter is close to the barrier height of the Cu structure.

Finally, since we are describing electron transport using a coherent formalism and have neglected inelastic scatterings, our results are only approximate at very high temperatures where the electron mean free path can become shorter than the barrier thickness. In practice, the electrical conductance and power factor should start decreasing

with T at high enough temperatures. We calculated the mean free path (MFP) of bulk MoSe<sub>2</sub> along the z-axis at different temperatures from first-principles to estimate the effect of inelastic electron-phonon scattering on the transport properties. The energy-dependent electron-phonon scattering rates and MFP is shown in Fig. 7. The electron mean free path at the bottom of the conduction band at 300K is 200Å and at 1000K is 35Å. The length of the 3 layers and 5 layers of MoSe<sub>2</sub> devices are 19.35Å and 32.25Å respectively. Therefore, up to 1000K, the inelastic electron-phonon scattering should not affect the performance of the 3 layers and 5 layers of MoSe<sub>2</sub> based SSTI devices.

#### IV. Conclusion

We used first-principle density functional theory (DFT) combined with real-space Green's functions formalism to evaluate the performance of SSTI devices with a varying number of MoSe<sub>2</sub> layers and with a variety of metallic electrodes. Among the studied metals, copper makes the lowest energy contact for electron transport while platinum makes low energy contact for hole transport with MoSe<sub>2</sub>. The Cu-3 MoSe<sub>2</sub>-Cu structure shows an extremely large PFT of 917 MWm<sup>-2</sup>K<sup>-1</sup> at 1200K which is the largest power factor calculated for thermionic structure based on TMDs. Since the barrier height can be tuned with the number of layers, we investigated the contact barrier dependence on the number of layers by studying the contact between gold and 3 to 6 layers of MoSe<sub>2</sub>. We found that Au with 3 layers of MoSe<sub>2</sub> shows the lowest barrier height, hence, makes better ohmic contact. Furthermore, we evaluated the performance of solid-state thermionic devices

with 3-6 layers of MoSe<sub>2</sub> sandwiched between two gold contacts and evaluated how their performance changes with the number of layers. Structures with 1 & 2 layers of MoSe<sub>2</sub> are not included as the transport in these structures is dominated by tunneling of carriers which is not desirable for SSTI devices. We find that SSTI devices with 3 layers of MoSe<sub>2</sub> show optimum performance at the temperature range of 200-500K and 970-1200K while devices with 4 and 5 layers of MoSe<sub>2</sub> show optimum performance at the temperature range of 500-750K and 750K-970K respectively. Therefore, the number of layers can be optimized for a given target operating temperature. Next, we studied the performance of two sets of asymmetric SSTI. Although an asymmetric metallic electrode enhances the efficiency of a VSTI device, we find that asymmetry of the electrode does not play any role in improving the performance of SSTI devices because the temperature difference across the device is very small, and one is in the linear regime. The most important parameter seems to be the energy barrier height and the structure with the lowest barrier height (0.10 eV) shows the highest performance. Finally, we estimated the electron mean free path at the Fermi level and across the MoSe<sub>2</sub> planes to be 200 Å, and 35Å at 300K and 1000K respectively which is larger than the thickness of the structures considered here.

## Acknowledgments

This work is supported by NSF grant number 1653268. MGR and KE acknowledge support from Hobby funding. The authors wish to acknowledge the Rivanna HPC system

of the University of Virginia and Extreme Science and Engineering Discovery Environment (XSEDE).

# References

- [1] A. Shakouri and J. E. Bowers, *Heterostructure Integrated Thermionic Coolers*, Appl. Phys. Lett. **71**, 1234 (1997).
- [2] G. D. Mahan, J. O. Sofo, and M. Bartkowiak, *Multilayer Thermionic Refrigerator and Generator*, J. Appl. Phys. **83**, 4683 (1998).
- [3] M. Markov and M. Zebarjadi, *Thermoelectric Transport in Graphene and 2D Layered Materials*, Nanoscale Microscale Thermophys. Eng. **23**, 117 (2019).
- [4] Y. Hishinuma, T. H. Geballe, B. Y. Moyzhes, and T. W. Kenny, *Refrigeration by Combined Tunneling and Thermionic Emission in Vacuum: Use of Nanometer Scale Design*, Appl. Phys. Lett. **78**, 2572 (2001).
- [5] M. G. Rosul, D. Lee, D. H. Olson, N. Liu, X. Wang, P. E. Hopkins, K. Lee, and M. Zebarjadi, *Thermionic Transport across Gold-Graphene-WSe* <sup>2</sup> van Der Waals Heterostructures, Sci. Adv. 5, (2019).
- [6] M. G. Rosul, M. S. Akhanda, and M. Zebarjadi, *Thermionic Energy Conversion*, in *Nanoscale Energy Transport* (IOP Publishing, 2020), pp. 14-1-14–29.
- [7] G. D. Mahan and L. M. Woods, *Multilayer Thermionic Refrigeration*, Phys. Rev. Lett. **80**, 4016 (1998).
- [8] M. Zebarjadi, Solid-State Thermionic Power Generators: An Analytical Analysis in the

- Nonlinear Regime, Phys. Rev. Appl. 8, 014008 (2017).
- [9] M. Zebarjadi, Solid-State Thermionic Power Generators: An Analytical Analysis in the Nonlinear Regime, Phys. Rev. Appl. 8, 014008 (2017).
- [10] Q. Li, Q. Hao, T. Zhu, M. Zebarjadi, and K. Takahashi, *Nanostructured and Heterostructured 2D Materials for Thermoelectrics*, Eng. Sci. **13**, 24 (2020).
- [11] A. Ziabari, M. Zebarjadi, D. Vashaee, and A. Shakouri, *Nanoscale Solid-State Cooling: A Review*, Reports Prog. Phys. **79**, 095901 (2016).
- [12] G. D. Mahan, Thermionic Refrigeration, J. Appl. Phys. **76**, 4362 (1994).
- [13] A. K. Geim and I. V Grigorieva, *Van Der Waals Heterostructures*, Nature **499**, 419 (2013).
- [14] J. E. Padilha, A. Fazzio, and A. J. R. da Silva, Van Der Waals Heterostructure of Phosphorene and Graphene: Tuning the Schottky Barrier and Doping by Electrostatic Gating, Phys. Rev. Lett. **114**, 066803 (2015).
- [15] A. L. Moore and L. Shi, Emerging Challenges and Materials for Thermal Management of Electronics, Mater. Today 17, 163 (2014).
- [16] X. Wang, M. Zebarjadi, and K. Esfarjani, First Principles Calculations of Solid-State

  Thermionic Transport in Layered van Der Waals Heterostructures, Nanoscale 8, 14695

  (2016).
- [17] X. Wang, M. Zebarjadi, and K. Esfarjani, High-Performance Solid-State Thermionic Energy Conversion Based on 2D van Der Waals Heterostructures: A First-Principles

- Study, Sci. Rep. 8, 9303 (2018).
- [18] P. Yuan, C. Li, S. Xu, J. Liu, and X. Wang, Interfacial Thermal Conductance between Few to Tens of Layered-MoS2 and c-Si: Effect of MoS2 Thickness, Acta Mater. 122, 152 (2017).
- [19] S. Vaziri, E. Yalon, M. Muñoz Rojo, S. V. Suryavanshi, H. Zhang, C. J. McClellan, C. S. Bailey, K. K. H. Smithe, A. J. Gabourie, V. Chen, S. Deshmukh, L. Bendersky, A. V. Davydov, and E. Pop, *Ultrahigh Thermal Isolation across Heterogeneously Layered Two-Dimensional Materials*, Sci. Adv. 5, eaax1325 (2019).
- [20] M. Massicotte, P. Schmidt, F. Vialla, K. Watanabe, T. Taniguchi, K. J. Tielrooij, and F. H. L. Koppens, *Photo-Thermionic Effect in Vertical Graphene Heterostructures*, Nat. Commun. 7, 12174 (2016).
- [21] X. Wang, M. Zebarjadi, and K. Esfarjani, High-Performance Solid-State Thermionic Energy Conversion Based on 2D van Der Waals Heterostructures: A First-Principles Study, Sci. Rep. 8, 9303 (2018).
- [22] S.-J. Liang, B. Liu, W. Hu, K. Zhou, and L. K. Ang, *Thermionic Energy Conversion Based on Graphene van Der Waals Heterostructures*, Sci. Rep. 7, 46211 (2017).
- [23] C.-C. Chen, Z. Li, L. Shi, and S. B. Cronin, Thermoelectric Transport across

  Graphene/Hexagonal Boron Nitride/Graphene Heterostructures, Nano Res. 8, 666

  (2015).
- [24] N. Poudel, S.-J. Liang, D. Choi, B. Hou, L. Shen, H. Shi, L. K. Ang, L. Shi, and S.

- Cronin, Cross-Plane Thermoelectric and Thermionic Transport across Au/h-BN/Graphene Heterostructures, Sci. Rep. 7, 14148 (2017).
- [25] N. Flöry, A. Jain, P. Bharadwaj, M. Parzefall, T. Taniguchi, K. Watanabe, and L. Novotny, *A WSe 2 /MoSe 2 Heterostructure Photovoltaic Device*, Appl. Phys. Lett. **107**, 123106 (2015).
- [26] G. Kioseoglou, A. T. Hanbicki, M. Currie, A. L. Friedman, and B. T. Jonker, *Optical Polarization and Intervalley Scattering in Single Layers of MoS2 and MoSe2*, Sci. Rep. **6**, 25041 (2016).
- [27] W. S. Yun, S. W. Han, S. C. Hong, I. G. Kim, and J. D. Lee, *Thickness and Strain Effects on Electronic Structures of Transition Metal Dichalcogenides:* 2H- MX2

  Semiconductors ( M = Mo, W; X = S, Se, Te), Phys. Rev. B **85**, 033305 (2012).
- [28] F. Léonard and A. A. Talin, Size-Dependent Effects on Electrical Contacts to Nanotubes and Nanowires, Phys. Rev. Lett. **97**, 026804 (2006).
- [29] Y.-F. Lin and W.-B. Jian, *The Impact of Nanocontact on Nanowire Based Nanoelectronics*, Nano Lett. **8**, 3146 (2008).
- [30] J. Kang, W. Liu, D. Sarkar, D. Jena, and K. Banerjee, *Computational Study of Metal Contacts to Monolayer Transition-Metal Dichalcogenide Semiconductors*, Phys. Rev. X 4, 031005 (2014).
- [31] J.-R. Chen, P. M. Odenthal, A. G. Swartz, G. C. Floyd, H. Wen, K. Y. Luo, and R. K. Kawakami, *Control of Schottky Barriers in Single Layer MoS 2 Transistors with*

- Ferromagnetic Contacts, Nano Lett. **13**, 3106 (2013).
- [32] S. Das, H.-Y. Chen, A. V. Penumatcha, and J. Appenzeller, *High Performance Multilayer MoS 2 Transistors with Scandium Contacts*, Nano Lett. **13**, 100 (2013).
- [33] M. Fontana, T. Deppe, A. K. Boyd, M. Rinzan, A. Y. Liu, M. Paranjape, and P. Barbara, *Electron-Hole Transport and Photovoltaic Effect in Gated MoS2 Schottky Junctions*, Sci. Rep. **3**, 1634 (2013).
- [34] M. Farmanbar and G. Brocks, *Controlling the Schottky Barrier at MoS2/Metal Contacts by Inserting a BN Monolayer*, Phys. Rev. B **91**, 161304 (2015).
- [35] M. Bokdam, G. Brocks, M. I. Katsnelson, and P. J. Kelly, *Schottky Barriers at Hexagonal Boron Nitride/Metal Interfaces: A First-Principles Study*, Phys. Rev. B **90**, 085415 (2014).
- [36] M. Bokdam, G. Brocks, and P. J. Kelly, Large Potential Steps at Weakly Interacting Metal-Insulator Interfaces, Phys. Rev. B **90**, 201411 (2014).
- [37] C. P. Y. Wong, C. Troadec, A. T. S. Wee, and K. E. J. Goh, *Gaussian Thermionic Emission Model for Analysis of Au/MoS2 Schottky-Barrier Devices*, Phys. Rev. Appl. **14**, 054027 (2020).
- [38] H. MOSS, Thermionic Diodes as Energy Converters, J. Electron. Control **2**, 305 (1957).
- [39] V. C. Wilson, Conversion of Heat to Electricity by Thermionic Emission, J. Appl. Phys. **30**, 475 (1959).
- [40] H. F. Webster, Calculation of the Performance of a High-Vacuum Thermionic Energy

- Converter, J. Appl. Phys. 30, 488 (1959).
- [41] J. M. Soler, E. Artacho, J. D. Gale, A. García, J. Junquera, P. Ordejón, and D. Sánchez-Portal, *The SIESTA Method for Ab Initio Order- N Materials Simulation*, J. Phys. Condens. Matter **14**, 2745 (2002).
- [42] J. P. Perdew, K. Burke, and M. Ernzerhof, *Generalized Gradient Approximation Made Simple*, Phys. Rev. Lett. 77, 3865 (1996).
- [43] J. P. Perdew, A. Ruzsinszky, G. I. Csonka, O. A. Vydrov, G. E. Scuseria, L. A. Constantin, X. Zhou, and K. Burke, *Restoring the Density-Gradient Expansion for Exchange in Solids and Surfaces*, Phys. Rev. Lett. **100**, 136406 (2008).
- [44] C. Huang, S. Wu, A. M. Sanchez, J. J. P. Peters, R. Beanland, J. S. Ross, P. Rivera, W. Yao, D. H. Cobden, and X. Xu, *Lateral Heterojunctions within Monolayer MoSe2-WSe2 Semiconductors*, Nat. Mater. **13**, (2014).
- [45] F. A. Rasmussen and K. S. Thygesen, Computational 2D Materials Database:

  Electronic Structure of Transition-Metal Dichalcogenides and Oxides, J. Phys. Chem. C

  119, (2015).
- [46] P. B. James and M. T. Lavik, *The Crystal Structure of MoSe*2, Acta Crystallogr. **16**, (1963).
- [47] S. Nayeb Sadeghi, M. Zebarjadi, and K. Esfarjani, Non-Linear Enhancement of Thermoelectric Performance of a TiSe 2 Monolayer Due to Tensile Strain, from First-Principles Calculations, J. Mater. Chem. C 7, 7308 (2019).

- [48] A. P. Nayak, S. Bhattacharyya, J. Zhu, J. Liu, X. Wu, T. Pandey, C. Jin, A. K. Singh, D. Akinwande, and J.-F. Lin, *Pressure-Induced Semiconducting to Metallic Transition in Multilayered Molybdenum Disulphide*, Nat. Commun. **5**, 3731 (2014).
- [49] M. Dion, H. Rydberg, E. Schröder, D. C. Langreth, and B. I. Lundqvist, *Van Der Waals Density Functional for General Geometries*, Phys. Rev. Lett. **92**, 246401 (2004).
- [50] J. Klimeš, D. R. Bowler, and A. Michaelides, Van Der Waals Density Functionals Applied to Solids, Phys. Rev. B 83, 195131 (2011).
- [51] M. Brandbyge, J.-L. Mozos, P. Ordejón, J. Taylor, and K. Stokbro, *Density-Functional Method for Nonequilibrium Electron Transport*, Phys. Rev. B **65**, 165401 (2002).
- [52] K. Esfarjani, M. Zebarjadi, and Y. Kawazoe, *Thermoelectric Properties of a*Nanocontact Made of Two-Capped Single-Wall Carbon Nanotubes Calculated within the

  Tight-Binding Approximation, Phys. Rev. B 73, 085406 (2006).
- [53] P. Giannozzi, S. Baroni, N. Bonini, M. Calandra, R. Car, C. Cavazzoni, D. Ceresoli, G. L. Chiarotti, M. Cococcioni, I. Dabo, A. Dal Corso, S. de Gironcoli, S. Fabris, G. Fratesi, R. Gebauer, U. Gerstmann, C. Gougoussis, A. Kokalj, M. Lazzeri, L. Martin-Samos, N. Marzari, F. Mauri, R. Mazzarello, S. Paolini, A. Pasquarello, L. Paulatto, C. Sbraccia, S. Scandolo, G. Sclauzero, A. P. Seitsonen, A. Smogunov, P. Umari, and R. M. Wentzcovitch, QUANTUM ESPRESSO: A Modular and Open-Source Software Project for Quantum Simulations of Materials, J. Phys. Condens.

- Matter **21**, 395502 (2009).
- [54] N. Troullier and J. L. Martins, *Efficient Pseudopotentials for Plane-Wave Calculations*, Phys. Rev. B **43**, 1993 (1991).
- [55] J. P. Perdew, K. Burke, and M. Ernzerhof, *Generalized Gradient Approximation Made Simple*, Phys. Rev. Lett. 77, 3865 (1996).
- [56] S. Poncé, E. R. Margine, C. Verdi, and F. Giustino, EPW: Electron–Phonon Coupling,

  Transport and Superconducting Properties Using Maximally Localized Wannier

  Functions, Comput. Phys. Commun. 209, 116 (2016).
- [57] F. Giustino, M. L. Cohen, and S. G. Louie, *Electron-Phonon Interaction Using Wannier Functions*, Phys. Rev. B **76**, 165108 (2007).
- [58] G. K. H. Madsen and D. J. Singh, *BoltzTraP. A Code for Calculating Band-Structure Dependent Quantities*, Comput. Phys. Commun. **175**, 67 (2006).
- [59] A. Rawat, N. Jena, D. Dimple, and A. De Sarkar, A Comprehensive Study on Carrier Mobility and Artificial Photosynthetic Properties in Group VI B Transition Metal Dichalcogenide Monolayers, J. Mater. Chem. A 6, 8693 (2018).
- [60] Z. Li, S. R. Bauers, N. Poudel, D. Hamann, X. Wang, D. S. Choi, K. Esfarjani, L. Shi, D. C. Johnson, and S. B. Cronin, *Cross-Plane Seebeck Coefficient Measurement of Misfit Layered Compounds (SnSe) n (TiSe 2 ) n (n = 1,3,4,5)*, Nano Lett. 17, 1978 (2017).